Showcasing research from Professor Miyamae's laboratory, Graduate School of Science and Engineering, Chiba University, Chiba, Japan.

Adhesion strength of aluminium surfaces coated with silane coupling protective layers *via* acid–base interactions

By combining sum-frequency generation (SFG) spectroscopy with molecular dynamics simulations, higher "acid hardness" of hydroxyl groups on silane-treated aluminium surfaces was found to enhance electrostatic interactions with amine-based curing agents in epoxy resins, leading to higher adhesive strength.

Image reproduced by permission of Takayuki Miyamae from *RSC Appl. Interfaces*, 2025, **3**, 364. The artwork has been partly generated by Google Gemini.

ROYAL SOCIETY
OF **CHEMISTRY**

rsc.li/RSCAppIInter

PAPER

Adhesion strength of aluminium surfaces coated with silane coupling protective layers *via* acid–base interactions

Kumpei Kobori,[a] Shuji Ogata, [iD] *[b] Shintaro Yamamoto,[c] Yusuke Takahashi[c] and Takayuki Miyamae [iD] *[ade]

Adhesive bonding, particularly with epoxy resins for lightweight metals such as aluminum, is crucial across various industries due to their excellent adhesion and stability. This study utilizes sum frequency generation (SFG) spectroscopy with model surfaces to examine the impact of the amine molecules in epoxy adhesives adsorbed onto aluminum surfaces. We investigated the Lewis acidity of the aluminum surfaces treated with three different silane agents—1,2-bis(triethoxysilyl)ethane (BTSE), octadecyltrimethoxysilane (OTS), and tetramethyl orthosilicate (TMOS)—by evaluating from the peak shifts of the surface hydroxyl groups observed in SFG using the Drago–Wayland method combined with the Badger–Bauer equation, and investigated the correlation with the respective adhesion characteristics. Our results reveal that the Lewis acidity (hardness of acid) of hydroxyl groups on the silane-treated surfaces is a critical factor in adhesive bonding. Surfaces treated with TMOS exhibit the hardest Lewis acid character, followed by BTSE and OTS, which directly correlated with the observed adhesion strengths. This suggests that stronger electrostatic interactions between the silane-treated surface (acting as a Lewis acid) and amine curing agents (acting as a Lewis base) enhance adhesion. Density-functional theory-based molecular dynamics simulations employing the H$^+$-shift method were used to investigate the acid dissociation constant (pK_α) of the hydroxyl group in TMOS and BTSE connected to HO-terminated γ-alumina. The calculated pK_α values showed a significant difference between single BTSE and bridged BTSE. Similarly, TMOS exhibited different acidic character depending on its adsorption forms. These findings suggest that the hydroxyl groups of bridged BTSE and the TMOS dimer show acidic character. These molecular-level insights indicate that when the hydroxyl groups are present on the surfaces, their adsorption states alter surface acidity, thereby impacting adhesion strength. Furthermore, these findings rationally explain well the previously observed amine segregation mystery at the adhesive interfaces in relation to adhesion strengths. These mechanism yields crucial insights for improving the adhesion and long-term stability of epoxy adhesives.

1 Introduction

Adhesive bonding technology has become more and more critical in a wide range of industrial fields.[1–3] From aircrafts, to automobiles and marine vessels, replacing rivets and bolts with adhesives greatly reduces weight and fuel consumption, thereby conserving energy, environmental resources, and cost.

Among various adhesives, epoxy resins cured with an amine curing agent are a prominent type of structural adhesive with excellent properties such as high adhesion strength, thermal stability, moisture stability, stiffness, and high insulating properties, and are used for jointing light weight metals such as aluminum. However, one of the key challenges facing adhesive bonding is the reduction or loss of adhesion strength under humid conditions. Although epoxy adhesives are often employed as adhesives to endure severe environments,[4,5] the adhesion strength between aluminum and epoxy resin decreases by 30 to 50% under moist conditions.[6–8] Unfortunately, it is extremely challenging to experimentally investigate the microscopic mechanism of weakening due to moisture.[9–11] This is because the interface is heterogeneous and because of the opaque nature of buried interfaces. Computational science offers a powerful approach to explore molecular interactions at buried adhesive

[a] Graduate School of Science and Engineering, Chiba University, 1-33 Yayoi-cho, Inage-ku, Chiba 263-8522, Japan. E-mail: t-miyamae@chiba-u.jp
[b] Graduate School of Engineering, Nagoya Institute of Technology, Gokiso-cho, Showa-ku, Nagoya 466-8555, Japan. E-mail: ogata@nitech.ac.jp
[c] Materials Research Laboratory, Technical Development Group, Kobe Steel Ltd. 5-5 Takatsukadai 1-chome, Nishi-ku, Kobe 651-2271, Japan
[d] Molecular Chirality Research Centre, Chiba University, 1-33 Yayoi-cho, Chiba-shi 263-8522, Japan
[e] Soft Molecular Activation Research Centre, Chiba University, 1-33 Yayoi-cho, Inage-ku, Chiba 263-8522, Japan

interfaces, which are difficult to examine experimentally. Major simulation techniques applied to adhesive bonding include density functional theory (DFT) calculations using fragment polymer models,[12–15] atomic dynamics simulations with empirical interatomic potentials,[16–18] and coarse-grained dynamics simulations.[19,20] Recently, Ogata *et al.* utilized first-principle DFT to reveal that the bond breakage of the protonated amine groups is the principal process causing the weakening of epoxy resins under wet conditions, and the amine group was protonated when the epoxy resin was stretched to a greater extent in water.[14,15]

Generally, when bonding metals, the surface condition of the metals greatly impacts adhesion strength.[1,2,21–25] Under atmospheric conditions, metal surfaces such as steel and aluminum are covered by a natural oxide layer, and the condition of the metal surface often becomes non-uniform due to the effects of the material components, processes such as rolling, extrusion, cutting, heating, and water-cooling during manufacturing, resulting in excessive growth of the oxide layer, structural defects, deterioration, corrosion, and other problems.[1,21,22] Furthermore, organic compounds derived from processing oils, packaging materials, and storage environments can adsorb onto the oxide layer, which significantly affect the adhesiveness of the metals. If these organic compounds remain on the adherend surface, the contact area between the adhesive and the adherend surface will decrease, preventing the adhesive from achieving its expected adhesion strength. Therefore, it is necessary to clean the surface of the adherend before bonding.[21,22] However, despite cleaning, the oxide layer readily adsorbs organic compounds and moisture from the atmosphere, causing surface conditions to change over time and resulting in variable adhesion strength. Therefore, to achieve stable adhesion strength, it is necessary to perform surface modification treatment to chemically stabilize the oxide film against fluctuations in temperature and humidity.[26] Indeed, European and American automobile manufacturers have made surface modification treatment standard in addition to surface cleaning for the purpose of improving the adhesion and storage stability of aluminum alloy oxide films, thereby ensuring long-term stability of adhesion strength.[27] To address this, a surface protective layer formed by surface treatment with silane agents, even those without reactive functional groups, has been recently reported.[26] Takahashi *et al.* reported that durability of adhesion strength between polyurethane or epoxy resin and aluminum substrates even in moisture is significantly improved.[26] However, the detailed adhesion mechanism of the surface functional groups by the silane agent treatment remains unclear.

Sum frequency generation (SFG) spectroscopy is a powerful technique for *in situ*, nondestructive observation of molecular interactions at the surface and interfaces.[28,29] Since SFG utilizes second-order nonlinear optical effects, it provides specific information about molecular functional groups at surfaces and interfaces where the inversion symmetry is necessarily broken.[30–33] SFG has been successfully applied to probe surfaces and buried interfaces of various polymer materials.[34–44] As the substrate is solid while the adhesive is in the liquid phase before curing, systematic attempts have been conducted to elucidate the adhesion mechanism during curing by understanding the interaction between the substrate surface and the adhesive, which causes the molecules in the adhesive to be specifically attracted to the interface. For analyzing the interaction at the adhesive interfaces, the method based on acid–base interactions[45–49] is highly effective for investigating the substrate-functional group interaction. Characterizing acid–base interactions based on the Drago–Wayland method[50] combined with the Badger–Bauer equation[51] by the pioneering work of Dhinojwala's group can help us better understand the aforementioned interfacial phenomena.[46–49]

In this study, we focus on silane coupling agents used as metal protection layers and investigate the interaction between silane-treated surfaces and amine molecules contained in epoxy adhesives using surface-specific vibrational SFG spectroscopy. The affinity between the adhesive and the protection layer is examined based on the acid–base interactions by comparing the adhesion strength of aluminum treated with three different silane agents: 1,2-bis(triethoxysilyl)ethane (BTSE), octadecyltrimethoxysilane (OTS), and tetramethyl orthosilicate (TMOS). BTSE is a silane coupling agent often used as a protective layer for the thin oxide films on chemically cleaned aluminum surfaces.[52] SFG spectroscopy is employed to characterize the surface properties of each silane agent treated surface using the Drago–Wayland method,[50] and to evaluate the interaction at the silane/epoxy interfaces. To achieve this, AlO_x thin-film-coated CaF_2 substrates serve as ideal aluminum surface models for SFG measurements. Aluminum surfaces that undergo chemical cleaning with acid and alkaline solutions are covered by a thin aluminum oxide layer, making them well-suited for studying the interaction between AlO_x and silane coupling agents, as well as for modeling silane-coated aluminum component surfaces. By conducting a detailed investigation using the Drago–Wayland method by Kurian *et al.*[46] into our silane modified systems, we find that the acidity (hardness of acid) of silane-treated surfaces plays a crucial role in electrostatic interaction with the amine compounds in epoxy adhesive, and positively correlates with adhesion strength to the epoxy adhesives. The hardness of the acid on the silane-treated surfaces is found for the first time to be positively correlated with the adhesion strength to epoxy adhesives. Furthermore, to verify the acid–base interaction on the silane-modified surfaces theoretically, molecular dynamics (MD) simulations with DFT calculations were performed utilizing γ-alumina as a model substrate, and the dissociated BTSE and TMOS surfaces positively exhibit acidity depending on the adsorption states, possessing an attractive effect on Lewis basic amines. These findings provide the first reasonable explanation for the previously puzzling interface segregation of amines at adhesive interfaces.[10,17]

© 2026 The Author(s). Published by the Royal Society of Chemistry

RSC Appl. Interfaces, 2026, **3**, 364–375 | 365

2 Acid–base interaction based on the Drago–Wayland method

The Drago–Wayland method[50] is a method for evaluating the interaction enthalpy based on Lewis acid–base theory. The Drago–Wayland equation is shown below,[50]

$$\Delta H_{ab} = E_a E_b + C_a C_b, \tag{1}$$

where E_a and E_b indicate the ease of electrostatic interaction between Lewis acids and Lewis bases, and C_a and C_b indicate the ease of covalent bonding, respectively. Then the interaction enthalpy ΔH_{ab} between materials can be evaluated from this equation. In addition, by combining the Drago–Wayland equation with the Badger–Bauer equation[51] shown in eqn (2), which obtains the interaction enthalpy ΔH_{ab} from the wavenumber shift Δv_{ab} in infrared spectroscopy, the surface properties focusing on Lewis acids on the surfaces can be determined.

$$\Delta H_{ab} = m\Delta v_{ab} + C. \tag{2}$$

The m and C parameters in eqn (2) are empirically determined constants for a particular functional group. Specifically, sample surfaces are put in contact with several solvents having known values of E_b and C_b, and the interaction enthalpy is obtained using eqn (2) of the Badger–Bauer equation from the Δv_{ab} of the surface vibrational mode observed in SFG that occurs when the functional groups of interest are in contact with the solvents. In this study, we focused on the peak wavenumber shift of the hydroxyl groups present on the silane coupling agent-treated surfaces when they were in contact with various solvents. Then, the values of E_a and C_a for each surface can be determined using the Drago–Wayland equation, and the surface Lewis acidity is identified.

3 Experimental

3.1 Chemicals

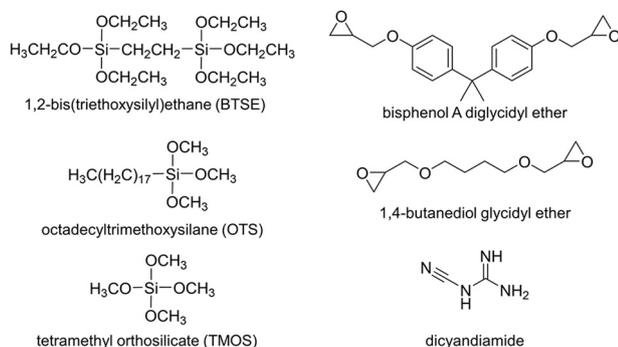The chemicals used in this study are shown in Fig. 1. 1,2-Bis(triethoxysilyl)ethane (BTSE, Tokyo Chemical Industry

Co., Ltd. Japan), octadecyltrimethoxysilane (OTS, Tokyo Chemical Industry Co., Ltd. Japan), and tetramethyl orthosilicate (TMOS, Tokyo Chemical Industry Co., Ltd. Japan) were used as surface protective layers for Al without further purification. The adhesive used was commercially available single-component epoxy adhesive XD911 (ref. 53) (DENATITE®, Nagase ChemteX) diluted with toluene. XD911 contains bisphenol A-type epoxy resin and 1,4-butanediol glycidyl ether as components, and dicyandiamide as a curing agent.

3.2 Characterization

The SFG system used in this study has been reported previously.[54] In these experiments, a mode-locked Nd:YAG laser (PL2251A-50, Ekspla, Lithuania) with a pulse width of 30 ps and repetition ratio of 50 Hz was used as the master laser source. The sample surface was irradiated with a tunable IR beam generated from the difference frequency generation unit (PG501-DFG2, EKSPLA, Lithuania) and 532 nm visible beam with the incident angles of 45° and 52°, respectively. The SFG spectra were collected in 5 cm^{-1} increments, and the data were averaged over 500 laser shots. The SFG spectra were collected using SSP (S-polarized sum frequency, S-polarized visible beam, and P-polarized IR beam) polarization combination under ambient conditions. The intensity of the SFG signal is as follows:[34]

$$I(\omega_{SF}) \propto \left| \chi_{NR}^{(2)} + \sum_q \frac{A_q}{\omega_{IR} - \omega_q + i\Gamma_q} \right|^2, \tag{3}$$

where $\chi_{NR}^{(2)}$ is the nonresonant contribution to the nonlinear susceptibility, and A_q, ω_q, and Γ_q are the amplitude, resonant frequency, and damping coefficient, respectively, of vibrational mode q.

The static contact angles of the surfaces treated with silane coupling agents were measured using an SImage AUTO 100 (Excimer, Inc., Japan). The contact angle was determined using the average value of at least three individual measurements.[55] X-ray photoelectron spectroscopy (XPS) measurements were performed using a JPS-9030 manufactured by JEOL Ltd. The X-ray source used in XPS was AlKα. Attenuated total reflection infrared (ATR-IR) measurements were performed using a Fourier transform infrared spectrometer (FT/IR-6600) manufactured by JASCO Co. with 128 accumulation cycles and a resolution of 4 cm^{-1}. A diamond prism was used for ATR measurements.

A tabletop tensile and compression tester (MCT-2150, A&D Company, Ltd., Japan) was utilized for the lap-shear tests. In this study, the adhesive strength was estimated by dividing the maximum value of the load–displacement curve by the adhesive area (7×3 mm^2). Therefore, the adhesive strength represents the stress at the sample break. The speed of the tensile test was adjusted to 100 mm min^{-1}. The thickness of the XD911 adhesive was controlled to be 100 μm using glass beads. The curing temperature of epoxy adhesives was 150 °C for 40 min. In addition to the adhesion strength of Al

Fig. 1 Chemical structures of the materials used in this study.

surfaces modified with three types of silane coupling agents, the adhesion strength of the epoxy adhesive on a cleaned Al substrate was also evaluated as a control. The adhesion strengths were determined by averaging at least eight independent test specimens. The error bars represent the standard errors of each surface treated test specimen.

3.3 Surface modification of Al using silane agents

For the lap-shear test specimens, all the 0.8 mm-thick Al A1050P test specimens (purity >99.5%) trimmed into 7 × 21 mm were first polished with the polishing compound and then cleaned with acetone for 30 min to degrease. These Al test specimens were then cleaned by chemical polishing as follows to completely remove surface contaminants. First, Al test specimens were immersed in a 10% aqueous solution of Es-clean AL-13 (Sasaki Chemical Co., Ltd. Japan) at 60 °C for 10 min, and then ultrasonicated with ultrapure water twice for 15 min. Then, the specimens were immersed in Es-clean AL-5000 (Sasaki Chemical Co., Ltd. Japan) at 80 °C for 3 min. The specimens were then ultrasonicated with ultrapure water twice for 15 min. The cleanliness of the Al surfaces was verified by the contact angle of water being almost zero. We noted that the contaminatants on the aluminum surfaces were completely removed and surface hydroxyl groups were present, as confirmed by XPS (Fig. S1) and ATR-IR (Fig. S2). The Si/Al atomic ratio of the silane coupling agents adsorbed on the Al surfaces were found to be almost the same for OTS and BTSE from the XPS. The ATR-IR spectra of the Al surfaces show that surface contamination has been completely removed as compared to the surface rinsed only with acetone. Furthermore, in the ATR-IR, the bands at 1130 cm^{-1} and 945 cm^{-1}, corresponding to Al(OH)$_3$ and Al$_2$O$_3$, respectively,[55] are clearly observed, indicating that the surface is covered with a thin oxide film with hydroxyl groups.

For the SFG experiments, a 3 mm-thick CaF$_2$ substrate (30 mmϕ, Pier Optics Co., Ltd., Japan) coated with 100 nm-thick AlO$_x$ was used. The AlO$_x$-coated CaF$_2$ was ultrasonicated in ethanol and acetone for 15 min each, followed by plasma treatment for 15 min using a plasma cleaner (PDC-32G, Harrick Plasma, USA) to remove surface contaminants. The cleanliness of the AlO$_x$-coated CaF$_2$ surfaces was confirmed by SFG to verify the absence of contamination (Fig. S3(d)).

Surface modification using silane coupling agents were performed by immersing chemically polished Al substrates and AlO$_x$-coated CaF$_2$ substrates in 1.5 mmol L^{-1} ethanol solution of each silane coupling agent with 30 μL acetic acid added for 24 h to prepare the silane coupling coatings. The samples were then ultrasonicated in ethanol for 15 min.

3.4 Simulation of the BTSE adsorbed surface

Lewis acid–base theory is centered on the principle that an acid accepts electrons from a base. When a proton is involved in this acid–base interaction, Brønsted–Lowry acid–base theory, which highlights proton transfer accompanied by electron transfer, becomes particularly relevant. According to

Brønsted–Lowry theory, the acidity of a compound can be assessed by determining the concentration of protons or H$_3$O$^+$ at equilibrium in water, represented by the acid dissociation constant (pK_α). Water molecules often play a role in these experiments to varying extents. Using pK_α as a measure of acidity is useful as well as practical, with values below 7 indicating acidity and those above 7 indicating basicity. In our study, we calculated the pK_α of BTSE under realistic conditions through first-principles simulations to determine its acidity in a specific setting. Here we outline the preparation process for the simulation system, where BTSE is connected to HO-terminated γ-alumina, to calculate the pK_α of the terminal –OH in BTSE. The detailed simulation system and the settings of DFT-MD simulation are described in the SI. The simulation model of the OH-terminated γ-alumina surface including 12 surface sites of Al$_2$–OH, 5 of Al–OHH, and 4 of Al–OH to mimic a HO-terminated γ-alumina is shown in Fig. 2(a) and (b). Subsequently, we connected fully hydrated BTSE, either in its single or p form (see Fig. 3(b)), to the HO-terminated γ-alumina. Here, we used the term "single-BTSE" to refer to a BTSE molecule that is isolated and bonded to the substrate surface, while "bridged-BTSE" to describe the process where two BTSE molecules first bond to the substrate surface and then subsequently bond to each other. Two Al-sites connecting the bridged BTSE are highlighted in yellow in Fig. 3(a). Additionally, H$_2$O
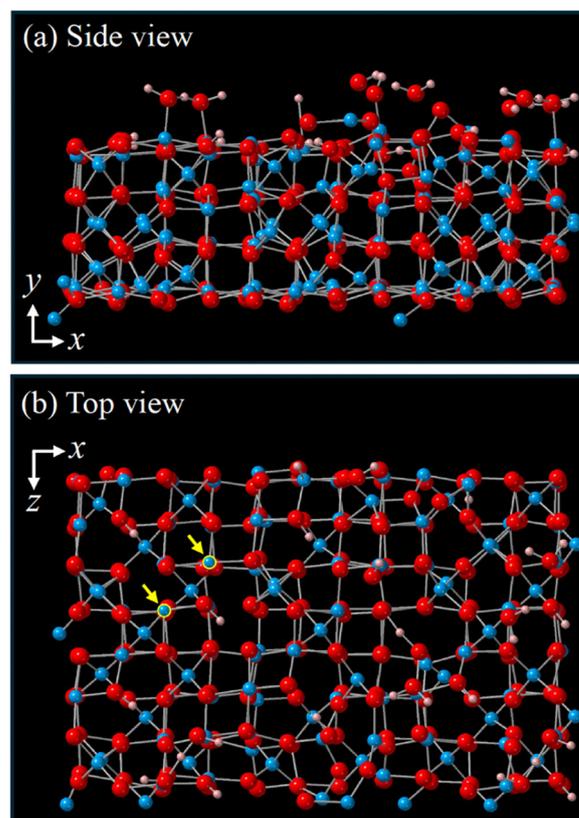

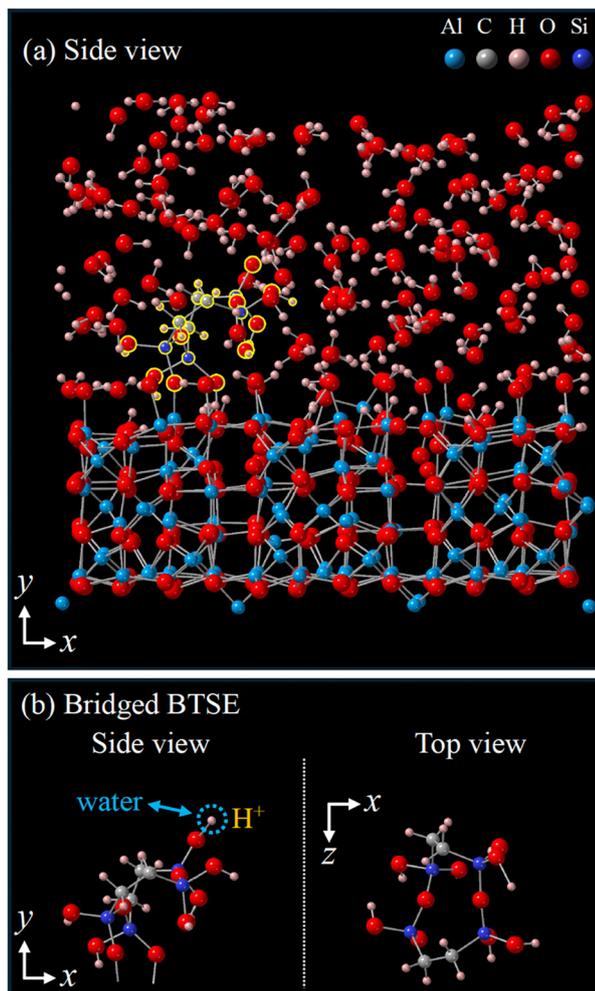**Fig. 2** Simulation model of HO-terminated γ-alumina. (a) Side view. (b) Top view.

Fig. 3 (a) Side view of simulation model of bridged BTSE connected to HO-terminated γ-alumina with liquid water at 297 K. The bridged BTSE (fully hydrated) is highlighted in yellow. (b) Zoom-in views of the bridged BTSE.

Fig. 4 Adhesion strength of Al substrates treated with OTS, BTSE, and TMOS with untreated Al substrates.

molecules were incorporated into the system, as depicted in Fig. 3(a). The present simulation system consisted of 865 atoms under periodic boundary conditions (PBCs). A virtual reflecting wall was positioned at the top-y of the simulation system to maintain a water density of 1.0 g cm^{-3} at 298 K. During the DFT-MD simulations, the two bottom-y layers of Al and O were kept fixed.

4 Results and discussion

4.1 Impact of silane coupling agents on the surfaces

First, the adhesion strengths of epoxy adhesives using Al test specimens adsorbed with OTS, BTSE, and TMOS silane coupling agents are presented in Fig. 4. For comparison, adhesion test results on clean Al substrates without silane treatments were also shown. Although the bonding conditions of the epoxy adhesive used are the same, significant differences in adhesion strength are observed depending on the silane agent used to form the ultrathin
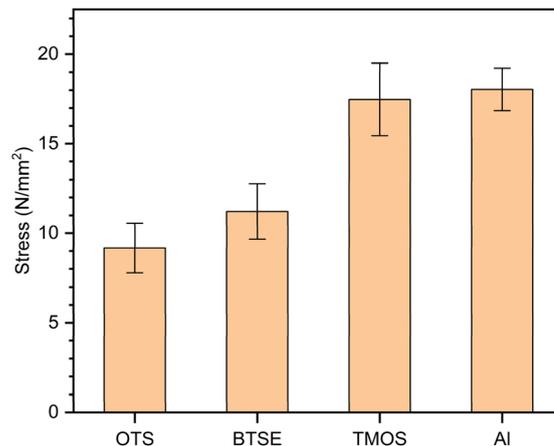
films on the Al surfaces. Therefore, the affinity of the epoxy adhesive varies depending on the type of silane agent used. The static water contact angles for chemically polished Al, 100 nm-thick AlO$_x$-coated CaF$_2$ without silane treatment, and AlO$_x$-coated CaF$_2$ surfaces modified with OTS, BTSE, and TMOS were approximately 0°, 0°, 69.3°, 62.7°, and 45.4°, respectively, indicating notable differences in surface hydroxyl group distribution across the surfaces.

To further investigate the surface condition of silane-treated surfaces, the hydroxyl groups on these silane-treated surfaces were analyzed using SFG spectroscopy under atmospheric conditions. CaF$_2$ substrates coated with a 100 nm-thick AlO$_x$ layer were used to observe the surface adsorbed with silane molecules. Fig. 5 presents the SSP-polarized SFG spectra collected under identical adsorption conditions. On AlO$_x$ surfaces without silane treatment, the band attributed to free OH groups appears at 3710 cm^{-1}, while broad bands of hydrogen-bonded OH bands, which are associated with adsorbed water, are observed from the 3000

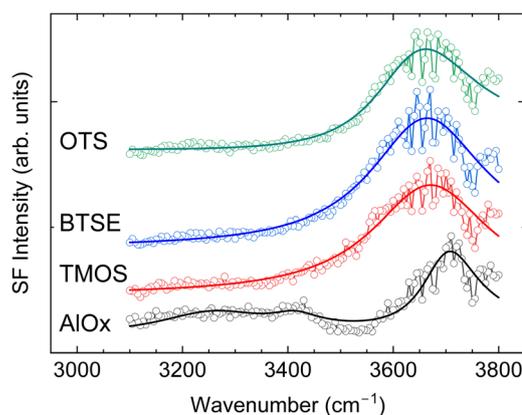**Fig. 5** SSP-polarized SFG spectra of 100 nm-thick AlO$_x$-coated CaF$_2$ substrates treated with OTS (green), BTSE (blue), and TMOS (red), along with the SFG spectrum of chemically polished AlO$_x$-coated substrates (black). Solid lines indicate the fitting curves. Spectra are offset for clarity.

to 3600 cm^{-1} region. In contrast, the OH band on silane-adsorbed surfaces shifts to approximately 3650 cm^{-1}, which shows a lower frequency shift and broader peak width compared to untreated AlO$_x$ surfaces. These spectral changes likely result from the interactions between hydrolyzed silane-derived OH groups and the alkyl groups. Notably, OH groups are scarcely detectable on OTS monolayers adsorbed onto glass surfaces, whereas they appear on OTS-adsorbed AlO$_x$ surfaces, suggesting differences in the alkyl chain orientation order between glass and AlO$_x$. This distinction is further validated by significant variations in SFG spectra within the CH stretching region (Fig. S3 and S4). The OTS adsorbed on glass exhibits distinct peaks originating from CH$_3$ in both SSP and PPP polarization combinations, indicating that the alkyl chains are in an all-*trans* orientation. In contrast, peaks from CH$_2$ are observed on AlO$_x$, suggesting the presence of a *gauche* structure. This indicates that alkyl chains exhibit a more disordered orientation on AlO$_x$. In other words, the adsorption behavior of silane agents on AlO$_x$ markedly differs from that on glass substrates. While silane coupling agents with alkyl chains tend to adopt a well-ordered orientation on glass and silicon oxide substrate surfaces, their adsorption behavior varies significantly on aluminum oxide and other metal substrates.[56–58] This conclusion is further supported by differences in water contact angles: 119° for OTS on glass *versus* 69° for OTS on AlO$_x$, underscoring substantial differences in wettability. Ultimately, when silane molecules adsorb onto AlO$_x$ surfaces, hydroxyl groups remain present to some extent, contributing to variations in surface chemistry and adsorption behavior.

Regarding BTSE, the ethoxy group is fully dissociated by adding a tiny amount of acetic acid during adsorption onto the AlO$_x$ surfaces. In the SFG spectra of BTSE adsorbed surfaces in Fig. S3 and S4, not only the CH$_3$-derived SFG peak disappears in SSP, but the methyl asymmetric stretching at 2970 cm^{-1} is also completely absent in PPP polarization. Thus, the peaks observed in the SFG spectra of BTSE is attributable to CH$_2$ within the molecules, not to undissociated ethoxy groups. On the SFG spectra of TMOS-adsorbed AlO$_x$ surfaces (Fig. S3), peaks corresponding to CH$_2$ and CH$_3$ groups are slightly observed. This is considered to be due to the residual ethanol on the surfaces. However, the TMOS surface exhibits sufficient adhesion strength as compared to Al, suggesting that the residual ethanol has a negligible impact on adhesion strength. Therefore, the influence of the trace amount of ethanol is not considered in the analysis. When the methoxy group on TMOS dissociates, the surface is covered with hydroxyl groups. This likely makes it difficult for adsorbed ethanol to desorb easily due to hydrogen bonding.

4.2 Acid–base interactions on surfaces treated with silane agents

Then, to investigate the Lewis acidity of these silane-treated surfaces, the SFG spectra were collected at the interfaces in
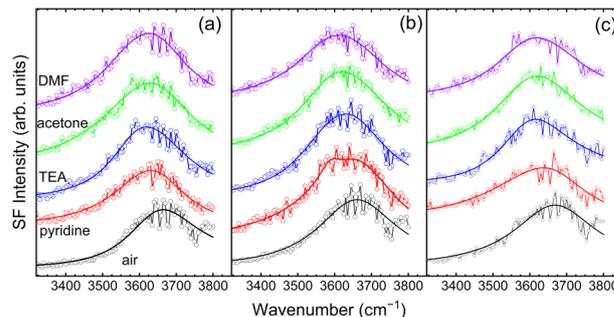

Fig. 6 SSP-polarized SFG spectra collected for four different liquids in contact with (a) OTS-treated, (b) BTSE-treated, and (c) TMOS-treated AlO$_x$ surfaces in the hydroxyl stretching region. The spectra have been fitted using eqn (3) and are shown alongside the collected spectra.

contact with silane-treated surfaces and four different Lewis base solvents. As shown in Fig. 6, peak positions of the OH band are red-shifted with respect to the peak position of the OH band observed at the air interfaces for all silane-treated surfaces. Observation of the peak shift of OH when the Lewis-basic solvents contact the substrates with hydroxyl groups corresponds well with the previously reported OH band peak shifts.[48,49] For comparison, we show the peak shift behavior of the OH band when AlO$_x$-coated CaF$_2$ is exposed to several solvents as shown in Fig. S5, and confirmed that the peak shift trends were consistent with previously reported results.[46,48] The peak position and the peak width (FWHM) of the surface hydroxyl band obtained from the fitting using eqn (3) are summarized in Tables 1 and S1. In the OH band fitting, two components were employed; the original band around 3650 cm^{-1} and a red-shifted band induced by contact with the liquids. We obtain the interaction enthalpy using

Table 1 Peak position (ω_q) and peak width (Γ_q) of the silane treated surfaces –OH peak observed in air and contact with organic solvents

OTS				
Solvent	ω_q (cm^{-1})	Γ_q (cm^{-1})	$\Delta\nu$ (cm^{-1})	ΔH_{ab} (kcal mol^{-1})
Pyridine	3592	108.7	55	0.63
Triethylamine	3591	97.9	56	0.64
Dimethylformamide	3589	131.6	58	0.66
Acetone	3604	166.3	43	0.50
Air	3647	117.5	0	—
BTSE				
Pyridine	3590	133.3	65	0.74
Triethylamine	3590	121.9	65	0.74
Dimethylformamide	3589	120.5	66	0.75
Acetone	3601	123.4	54	0.62
Air	3655	131.9	0	—
TMOS				
Pyridine	3597	161.0	68	0.77
Triethylamine	3593	115.0	72	0.81
Dimethylformamide	3598	119.4	67	0.76
Acetone	3604	140.1	61	0.69
Air	3665	136.8	0	—

© 2026 The Author(s). Published by the Royal Society of Chemistry

*RSC Appl. Interfaces*, 2026, **3**, 364–375 | **369**

the Drago–Wayland[50] and Badger–Bauer equations,[51] which are based on acid–base interactions, for the frequency shift of the hydroxyl groups when the hydroxyl groups on the silane-treated surfaces are in contact with various Lewis bases. By combining the Drago–Wayland method,[50] which obtains the interaction enthalpy ΔH_{ab} between materials, and the Badger–Bauer equation,[51] which evaluates the ΔH_{ab} from the frequency shift Δv_{ab} in infrared spectroscopy, we obtained the ΔH_{ab} at the silane-treated surfaces. For the calculation, E_b and C_b values are taken from the literature values.[46,48] Using these values, we then determined the relative strengths of the electrostatic interactions on each silane-treated surface. Fig. 7 shows a plot of $\Delta H_{ab}/C_b$ as a function of E_b/C_b. From Fig. 7, The E_a and C_a of AlO$_x$ surfaces treated with OTS, BTSE, and TMOS are $E_a^{OTS} = 8.7 \times 10^{-4}$ and $C_a^{OTS} = 5.07 \times 10^{-1}$, $E_a^{BTSE} = 11.3 \times 10^{-4}$ and $C_a^{BTSE} = 5.93 \times 10^{-1}$, and $E_a^{TMOS} = 15.8 \times 10^{-4}$ and $C_a^{TMOS} = 6.19 \times 10^{-1}$, respectively. In addition, from these values, E_a/C_a is 1.7×10^{-3} for OTS, 1.9×10^{-3} for BTSE, and 2.6×10^{-3} for TMOS, respectively. A high E_a/C_a value indicates that the hydroxyl groups on the surface is a hard Lewis acid, and TMOS-treated surface exhibits the hardest Lewis acid character, followed by BTSE and OTS in the order of increasing Lewis acidity. Since the hardness of the Lewis acid indicates the ease with which charge interactions, *i.e.*, electrostatic interactions, occur, this result indicates that AlO$_x$ surfaces treated with TMOS or BTSE have stronger electrostatic interactions than that those treated with OTS.

Next, in Fig. 8, we present the SFG spectra of these three silane-treated surfaces in contact with 10 wt% dicyandiamide–DMF solution. Dicyandiamide is one of the most widely used latent hardeners for epoxy resins and serves as the primary agent for high-temperature curing of one-component epoxy adhesive formulations. The fitting summary is shown in Table S2. A slight amine stretching vibration can be observed around 3300 cm^{-1} at the interface with the dicyandiamide–DMF solution for all silane-treated surfaces, though the signal-to-noise ratio is not good. For comparison, Fig. 8 also shows the SFG spectra of the OH region when DMF without dicyandiamide is in contact with
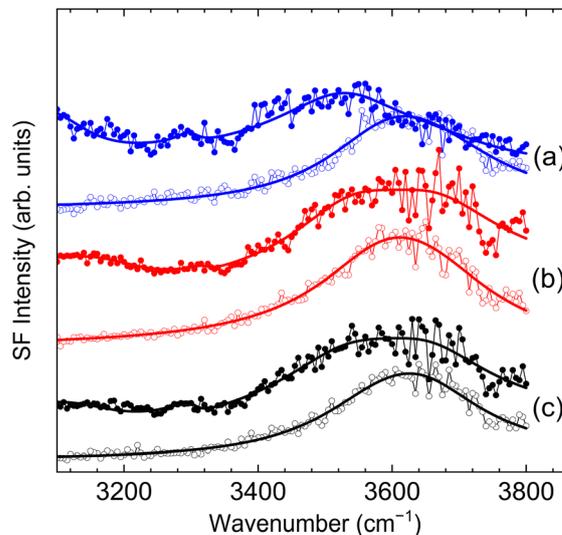
Fig. 8 SFG spectra collected for DMF and 10 wt% dicyandiamide–DMF solution in contact with (a) TMOS-treated (blue), (b) BTSE-treated (red), and (c) OTS-treated (black) AlO$_x$ surfaces. Open circles represent the SFG spectra at the interfaces between three different silane-treated surfaces and DMF, while filled circles correspond to spectra obtained when the samples were in contact with the 10 wt% dicyandiamide–DMF solution. SFG intensities have been normalized to highlight the shift in peak positions. Solid lines indicate the fitting curves using eqn (3).

each silane-treated surface. The presence of the peak at 3300 cm^{-1} is evident by comparing with the SFG spectra of the DMF interfaces without dicyandiamide. When the dicyandiamide–DMF solution contacts these silane-treated surfaces, the OH peak position undergoes a significant red-shift in the order described above. The OH band positions for the silane-treated surfaces, when in contact with a dicyandiamide solution, showed red shifts of 42 cm^{-1} for OTS, 42 cm^{-1} for BTSE, and 59 cm^{-1} for TMOS, respectively, compared to the OH peak positions obtained with DMF interfaces. Based on these results, the acid hardness of the surface hydroxyl groups on the silane-treated surfaces differs among the silane-treated surfaces. Consequently, we conclude that the difference in the adhesion strength shown Fig. 4 is the reason for the difference in the acid hardness of the residual surface hydroxyl groups on the silane-treated surfaces. The curing agent, which contains amines classified as Lewis bases, is attracted to the surface hydroxyl groups on the silane-treated surfaces, which are thought to be Lewis acids, through acid–base interactions. This mechanism can explain the variations in adhesion strength associated with different silane agents. In recent years, advances in analytical techniques and computational science have frequently revealed the segregation of nitrogen atoms derived from amines at epoxy adhesive interfaces.[10,17,59–62] When the substrate surfaces exhibit Lewis acidity, this characteristic provide a reasonable explanation for the concentration of amines at the interfaces during epoxy adhesive curing.
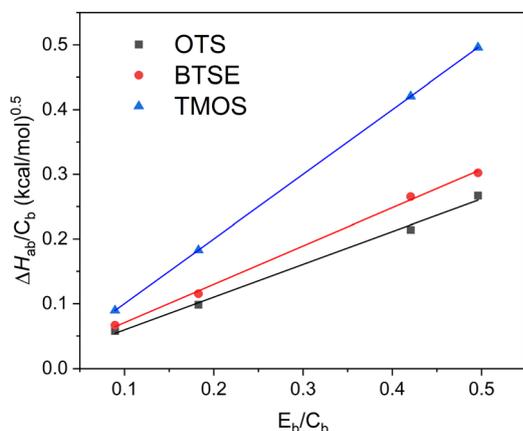

Fig. 7 $\Delta H_{ab}/C_b$ plot as a function of E_b/C_b. Solid lines are linear fit.

4.3 The H$^+$-shift method to calculate pK_α with DFT-MD simulation

Since BTSE molecules have two Si(OCH$_2$CH$_3$)$_3$ groups, it is necessary to determine the adsorption configuration on the AlO$_x$ surface when they are dissociated. We adopted the configuration shown in Fig. 3 obtained *via* DFT-MD simulation at 298 K to evaluate the pK_α of BTSE connected to the surface. Experimentally, it has been suggested that the BTSE-treated surface exhibits Lewis acidity, but a detailed investigation of its origin is essential to understand the nature of acid–base interactions on the surface.

The H$^+$-shift method[15] was applied to calculate the pK_α with DFT-MD simulation. The acid dissociation of compound AH in water

$$AH(aq) + \delta F_{AH} = A^-(aq) + H^+(aq) \quad (4)$$
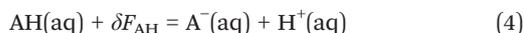
was initially considered with the H$^+$-dissociation free energy δF_{AH}. The acid dissociation constant pK_α of AH is then defined as

$$pK_\alpha = \delta F_{AH}/(\ln 10 \cdot k_B T) \quad (5)$$

where T is the temperature and k_B is the Boltzmann constant. The solvated proton H$^+$(aq) migrates in water by changing the H$_2$O molecule to which it is adsorbed.

The H$^+$ ion adsorbs onto a single H$_2$O molecule to form the Eigen core of H$_3$O$^+$(aq), and then repeatedly migrates with a timescale of 1 ps to neighboring H$_2$O molecules through the formation of the Zundel core structure (H$_2$O·H$^+$·OH$_2$).[63] In the H$^+$-shift method,[15] configuration samplings of the solvation structure were conducted for H$_3$O$^+$(aq) by suppressing the H$^+$ migration in the DFT-MD simulation. The free-energy difference between H$^+$(aq) and H$_3$O$^+$(aq) is approximated considering the translation free-energy of H$^+$ as

$$H^+(aq) + H_2O(aq) = H_3O^+(aq) + k_B T \ln\left(C_0 \lambda_{H^+}^3\right). \quad (6)$$

Here, the thermal de Broglie wavelength $\lambda_{H^+} = h/\sqrt{2\pi m_{H^+} k_B T} = 1.0077$ Å and $\ln\left(C_0 \lambda_{H^+}^3\right) = -7.3918$ for $C_0 = 1$ mol/(0.1 m)^3, the mass $m_{H^+} = 1.6725 \times 10^{-27}$ kg, and $T = 298$ K for the standard state. Eqn (4) can be rewritten using eqn (6) as

$$AH(aq) + H_2O(aq) + \Delta F_{AH} = A^-(aq) + H_3O^+(aq) \quad (7)$$
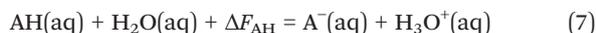
with

$$\Delta F_{AH} = \delta F_{AH} - k_B T \ln\left(C_0 \lambda_{H^+}^3\right). \quad (8)$$

ΔF_{AH} is the free energy required to shift H$^+$ from AH to an H$_2$O molecule to form a stable H$_3$O$^+$(aq), which is obtained *via* two subprocesses: (i) and (ii) as $\Delta F_{AH} = \Delta F_{AH}^{(i)} + \Delta F_{AO}^{(ii)}$ as explained below.

When an H$_3$O$^+$ in water is gradually shifted to A$^-$(aq) from a mutually well-separated position, the H$_3$O$^+$ initially experiences repulsive forces due to breaking of water-solvation and subsequently attractive forces prior to its dissociation to transfer H$^+$ to A$^-$(aq). This metastable state is denoted as A$^-$(aq)·H$_3$O$^+$(aq). Based on this consideration, the H$^+$-transfer process was divided into two subprocesses: (i) a subprocess changing between the states of AH(aq) + H$_2$O(aq) and A$^-$(aq)·H$_3$O$^+$(aq), and (ii) a subprocess between the states of A$^-$(aq)·H$_3$O$^+$(aq) and A$^-$(aq) + H$_3$O$^+$(aq). Corresponding free-energy changes $\Delta F_{AH}^{(i)}$ and $\Delta F_{AO}^{(ii)}$ for subprocesses (i) and (ii) are calculated by thermodynamic integration of the applied work:

$$\Delta F_{AH}^{(i),(ii)} = -\frac{1}{2} \int_{\text{initial}}^{\text{final}} \left\langle \vec{f}_{ij} \cdot \hat{n}_{ij} \right\rangle dr_{ij}. \quad (9)$$

Here the inter-atomic distance $r_{ij} = |\vec{r}_{ij}| = |\vec{r}_i - \vec{r}_j|$ between atom-i and atom-j is fixed using the RATTLE method[64] during the time average $\langle \cdots \rangle$ in DFT-MD sampling, $\hat{n}_{ij} = \vec{r}_{ij}/r_{ij}$ and $\vec{f}_{ij} = \vec{f}_i - \vec{f}_j$. Thus, the atomic pair (i, j) was set as (A$^-$, H$^+$ of H$_3$O$^+$) for subprocess (i) and (A$^-$, O of H$_3$O$^+$) for subprocess (ii) to have better sampling statistics for $\vec{f}_{ij}$. Auxiliary inter-atomic potentials v_{support} were added to the system, which does not create additional atomic forces in both the initial and final states and therefore does not affect the calculated value of $\Delta F_{AH}^{(i),(ii)}$. With the incorporation of v_{support}, no H$^+$-transfer between mutually neighboring H$_2$O molecules nor between H$_2$O and A$^-$ occurred.

The numerical integration in eqn (9) and its error analysis were performed as follows. Without loss of generality, we consider a numerical integration $\int_{r_{\text{init}}}^{r_{\text{final}}} g(r) dr$ of a time-fluctuating quantity $g(r)$. For this purpose, we set discrete n-points $r_i = r_{\text{init}} + i\Delta r$ with $\Delta r = (r_{\text{final}} - r_{\text{init}})/n$ for $i = \{0, 1, \ldots, n\}$ in the range $[r_{\text{init}}, r_{\text{final}}]$; extension to the case of non-uniform discrete points is straightforward. We sample $g_i \equiv g(r_i)$ for a given r_i at every timestep through a DFT-MD simulation run to find the time-averaged value $\bar{g}_i$. We conduct the integration $\int_{r_{\text{init}}}^{r_{\text{final}}} g(r) dr$ using $\{\bar{g}_i\}$ by the trapezoidal rule:

$$I_T \equiv \frac{\Delta r}{2} \Delta r \bar{g}_0 + \Delta r \sum_{i=1}^{n-1} \bar{g}_i + \frac{\Delta r}{2} \Delta r \bar{g}_n. \quad (10)$$

The standard error $s(I_T)$ of I_T relating to the time-fluctuation of g_i is evaluated through the well-known error propagation formula as

$$s(I_T)^2 = \left(\frac{\Delta r}{2}\right)^2 s_0^2 + (\Delta r)^2 \sum_{i=1}^{n-1} s_i^2 + \left(\frac{\Delta r}{2}\right)^2 s_n^2. \quad (11)$$

Here the standard error s_i is obtained using 1.0 ps-averaged data of g_i.[65] The $s(I_T)$ was used to evaluate the possible error of pK_α. We add that the integration using the Simpson's rule gave no substantial change in the results in the present calculation of eqn (9).

The H$^+$-shift method was applied to liquid water (128 H$_2$O molecules) under the PBCs at 298 K simulated using the real-

© 2026 The Author(s). Published by the Royal Society of Chemistry

RSC Appl. Interfaces, 2026, **3**, 364–375 | 371

space-grid type DFT code (DC-RGDFT), $\Delta F_{H_2O}^{(i)} = 1.215 \pm 0.015$ eV for subprocess (i) and $\Delta F_{H_2O}^{(ii)} = -0.134 \pm 0.003$ eV for subprocess (ii), that is, $\Delta F_{H_2O} = \Delta F_{H_2O}^{(i)} + \Delta F_{H_2O}^{(ii)} = 1.081 \pm 0.015$ eV.[15] This corresponds to pK_α 15.1 ± 0.3. Comparing with the experimental value of $-\log_{10}\frac{[H^+][OH^-]}{[H_2O]} = -\log_{10}\frac{10^{-14}}{55} = 15.7$, we anticipate that the H$^+$-shift method with DC-RGDFT gives pK_α within a possible deviation of ~0.5.

4.4 Predicted pK_α for –OH of BTSE connected to HO-terminated γ-alumina

We calculated pK_α of an –OH in BTSE connected to HO-terminated γ-alumina using the H$^+$-shift method (see section 4.2). The –OH for the bridged BTSE, depicted in Fig. 3(b), corresponds to "AH" in eqn (7), the deprotonated state –O$^-$ to "A$^-$". The temperature was maintained at 298 K to calculate $\Delta F_{NH} = \Delta F_{NH}^{(i)} + \Delta F_{NO}^{(i)}$ for deprotonation of the H$^+$ from the –OH.

To calculate the free-energy change $\Delta F_{NH}^{(i)}$, an H$_3$O$^+$ ion was initially prepared close to the target O$^-$ in water by

Fig. 9 (Top) Definitions of $\vec{r}_{OH}$ and $\vec{r}_{OO}$ used in the H$^+$-shift method to calculate the deprotonation free energy of –OH in BTSE connected to HO-terminated γ-alumina. (Middle) The DFT-MD sampling result of $\langle \vec{f}_{OH} \cdot \hat{n}_{OH} \rangle$ at each r_{OH} for subprocess (i) in the H$^+$-shift method. (Bottom) Same as the Middle, but of $\langle \vec{f}_{OO} \cdot \hat{n}_{OO} \rangle$ at each r_{OO} for subprocess (ii).

shifting H$^+$ from –OH to H$_2$O with a distance of r_{OH} = 1.8 Å between the O$^-$ and the closest H$^+$ of H$_3$O$^+$, where the H$^+$ experiences a weak attractive force from the O$^-$, i.e., $\vec{f}_{OH} \cdot \hat{n}_{OH} < 0$. Zoom-in views of representative configurations are shown in Fig. 9 (top). The value of r_{OH} was then changed in a stepwise manner to find two extreme values of r_{OH}, where the time-average of $\vec{f}_{OH}$ is zero, the shorter extreme value corresponds to the state AH(aq) + H$_2$O(aq), and the longer extreme value corresponds to the metastable state A$^-$(aq)·H$_3$O$^+$(aq). At each value of r_{OH}, a simulation run was performed for 6.0–8.0 ps after the relaxation run of about 3.0 ps. The 1.0 ps-block averaged values were used to evaluate the standard errors. The time-averaged values, $\langle \vec{f}_{OH} \cdot \hat{n}_{OH} \rangle$, are plotted in Fig. 9 (middle), which were used for the integration in eqn (9). We thereby obtained $\Delta F_{NH}^{(i)}$ = 0.762 ± 0.031 eV for the single BTSE and 0.697 ± 0.025 eV for the bridged BTSE.

For the calculation of the free-energy change $\Delta F_{NH}^{(ii)}$, the metastable state found in subprocess (i) (i.e., A$^-$(aq)·H$_3$O$^+$(aq)) was used as the starting point, wherein the value of r_{OO} between the O$^-$ and the O of H$_3$O$^+$ was set at 3.0–3.3 Å and $\langle \vec{f}_{OO} \rangle$ = 0. Similar to subprocess (i), the r_{OO} was extended stepwise until $\langle \vec{f}_{OO} \cdot \hat{n}_{OO} \rangle$ = 0 at r_{OO} = 3.7–3.9 Å. The time-averaged values, $\langle \vec{f}_{OO} \cdot \hat{n}_{OO} \rangle$, shown in Fig. 9 (bottom) were used for the integration in eqn (9). The calculated values were $\Delta F_{NH}^{(ii)}$ = −0.026 ± 0.005 eV for the single BTSE and −0.273 ± 0.006 eV for the bridged BTSE.

From the subprocesses (i) and (ii), we found $\Delta F_{NH} = \Delta F_{NH}^{(i)} + \Delta F_{NO}^{(ii)}$ = 0.736 ± 0.031 eV for the single BTSE and 0.423 ± 0.026 eV for the bridged BTSE. Adding the translational free-energy of an H$^+$ ion, we obtained pK_α of the –OH as 9.24 ± 0.5 for the single BTSE and 3.94 ± 0.5 for the bridged BTSE. In contrast, for bridged-BTSE, where one ethoxy group is undissociated, the pK_α value was 11.2 ± 0.5 indicating that complete dissociation of the ethoxy group is effective for enhancing surface acidity. By taking into account the inherent error ~0.5 in pK_α by the H$^+$-shift method with DC-RGDFT (see section 4.3), we conclude that the –OH of the bridged BTSE connected to HO-terminated γ-alumina is acidic, while that of single BTSE is basic. These results suggest that bridged BTSE interacts more effectively with Lewis basic molecules contained in adhesives. We also calculated the pK_α of the dissociated TMOS connected to HO-terminated γ-alumina in three forms (see Fig. S6). For dimerized TMOS, the calculated pK_α is 3.81 ± 0.5, which is significantly smaller than 8.32 ± 0.5 (9.14 ± 0.5) for single (bridged) TMOS. It is well established experimentally that monomer Si(OH)$_4$ readily dimerizes in water.[66] Consequently, the dimerized form of TMOS is anticipated on HO-terminated γ-alumina. Given that the acidity of dimerized TMOS and bridged BTSE is approximately equivalent, we propose that the observed higher acidity of TMOS compared to BTSE in the current experiments is due to the potentially higher smoothness of the TMOS-connected γ-alumina surface, attributed to the smaller size of TMOS relative to BTSE. This finding supports their superior adhesion to epoxy adhesives.

Conclusions

This study successfully employed surface-specific vibrational SFG spectroscopy, combined with the Drago–Wayland and Badger–Bauer equations, to elucidate the critical role of surface chemistry in determining the adhesion strength of epoxy resins on silane-treated aluminium surfaces. Despite identical bonding conditions, adhesion strength varied significantly depending on the silane agent used to modify the aluminium oxide surface.

Our investigations revealed that the Lewis acidity, or "*hardness*", of the hydroxyl groups present on the silane-treated surfaces is a crucial factor influencing adhesive performance. TMOS-treated surfaces exhibited the hardest Lewis acid character, followed by BTSE and then OTS. Crucially, this hierarchy of Lewis acidity directly correlated with the observed adhesion strengths, demonstrating that surfaces with harder Lewis acid facilitate stronger bonding.

The interaction analysis with a representative amine curing agent (dicyandiamide) further validated this mechanism, showing distinct spectral shifts indicative of acid–base interactions. These findings strongly suggest that enhanced electrostatic interactions between the Lewis acidic hydroxyl groups on the modified surface and the Lewis basic amine curing agents are key to improving adhesion. This molecular-level insight offers a comprehensive explanation for variations in adhesion strengths across different surface treatments and aligns with previous observations of amine segregation at adhesive interfaces during curing.

Furthermore, a simulation system of BTSE or TMOS connected to HO-terminated γ-alumina was successfully employed to investigate the pK_α of the hydroxyl group in BTSE and TMOS using the H^+-shift method with DFT-MD simulations. The H^+-shift method allowed for the calculation of the pK_α by determining the free energy required to shift a proton from AH to an H_2O molecule, which was divided into two subprocesses involving the displacement of H^+ and H_3O^+ ions. Numerical integration with error analysis was performed to ensure the reliability of the calculated free-energy changes. The calculated pK_α values for the hydroxyl group of BTSE connected to HO-terminated γ-alumina revealed a significant difference between the single and bridged BTSE forms. Specifically, the single BTSE exhibited a pK_α of 9.24 ± 0.5, while the bridged BTSE showed a pK_α of 3.94 ± 0.5. For dimerized TMOS, the calculated pK_α is 3.81 ± 0.5, which is significantly smaller than 8.32 ± 0.5 (9.14 ± 0.5) for single (bridged) TMOS. Accounting for an inherent error of approximately 0.5 in the H^+-shift method with DC-RGDFT, these results strongly suggest that the –OH group of bridged BTSE and dimerized TMOS connected to HO-terminated γ-alumina is acidic, whereas that of single BTSE and single (bridged) TMOS is rather basic.

SFG experiments clarified that the TMOS-treated and BTSE-treated AlO_x surfaces exhibit Lewis acidity. In addition, DFT-MD calculations revealed that the bridged BTSE connected to OH groups on the AlO_x surface was more acidic than BTSE with a single form. These results demonstrate that the adsorption configuration of each silane agent and the resulting Lewis acidity of the hydroxyl groups are crucial for molecular reactivity during adhesion. Ultimately, this work provides valuable insights into the fundamental interactions at buried adhesive interfaces, which are essential for the rational design and development of stable, durable, and high-performance epoxy adhesive systems. This understanding is particularly relevant for applications in humid environments, where maintaining adhesion integrity is often challenging.

Author contributions

The manuscript was written through contributions of all authors. All authors have given approval to the final version of the manuscript. K. K., S. O., S. Y., Y. T. and T. M. conceived the research. K. K. and T. M. carried out the sample preparation, data curation and analyses. S. O. conducted the DFT-MD simulations. K. K., S. O., S. Y., Y. T. and T. M. wrote the original draft, K. K., S. O. and T. M. reviewed and edited the draft. S. O. and T. M. supervised the research, established funding for the research, and provided contributions to the interpretation of the results.

Conflicts of interest

There are no conflicts to declare.

Data availability

The data supporting this article have been included in the SI. Supplementary information (SI): simulation system to analyse acidity: BTSE connected to HO-terminated γ-alumina, settings of DFT-MD simulation, XPS spectra of the chemically polished Al substrate, OTS-treated and BTSE-treated samples, ATR-IR spectra of Al and chemically polished Al substrates, SSP and PPP polarized SFG spectra of silane-treated AlO_x substrates, SSP polarized SFG spectra of OTS and BTSE adsorbed on glass or AlO_x substrates, SSP polarized SFG spectra for five different liquids in contact with AlO_x substrate without silane-treatment, DFT-MD sampling result of single, bridged, and dimerized forms of TMOS connected to HO-terminated γ-alumina, fitting summary tables for SFG spectra in Fig. 6 and 8. See DOI: https://doi.org/10.1039/d5lf00336a.

Acknowledgements

© 2026 The Author(s). Published by the Royal Society of Chemistry

RSC Appl. Interfaces, 2026, **3**, 364–375 | 373

Notes and references

1 R. D. Adams, *Adhesive Bonding: Science, Technology and Applications*, Woodhead Publishing Limited, Cambridge, 2005.

2 T. A. Barnes and I. R. Pashby, *J. Mater. Process. Technol.*, 2000, **99**, 72–79.

3 S. N. Wang, Y. Li, Y. M. Guo, B. Cai, B. G. P. Zhang, Z. X. Liu and P. C. Wang, *Int. J. Adhes. Adhes.*, 2019, **90**, 38–46.

4 A. I. Gagani, A. E. Krauklis, E. Sæter, N. P. Vedvik and A. T. Echtermeyer, *Compos. Struct.*, 2019, **220**, 431–440.

5 A. Ilioni, P. Le Gac, C. Badulescu, D. Thévenet and P. Davies, *J. Adhes.*, 2019, **95**, 64–84.

6 D. M. Brewis, J. Comyn and J. L. Tegg, *Int. J. Adhes. Adhes.*, 1980, **1**, 35–39.

7 K. Nakamura, T. Ueda, S. Hosono and T. Maruno, *Int. J. Adhes. Adhes.*, 1987, **7**, 209–212.

8 Y. Tomita, I. Shohji, S. Koyama and S. Shimizu, *Procedia Eng.*, 2017, **184**, 231–237.

9 S. Cotugno, G. Mensitieri, P. Musto and L. Sanguigno, *Macromolecules*, 2005, **38**, 801–811.

10 H. Yamane, M. Oura, N. Yamazaki, T. Ishihara, K. Hasegawa, T. Ishikawa, K. Takagi and T. Hatsui, *Sci. Rep.*, 2022, **12**, 16332.

11 S. Horiuchi, N. Terasaki and T. Miyamae, *Interfacial Phenomena in Adhesion and Adhesive Bonding*, Springer Nature, Singapore, 2023.

12 C. Higuchi, H. Tanaka and K. Yoshizawa, *J. Comput. Chem.*, 2019, **40**, 164–171.

13 S. Nakamura, Y. Tsuji and K. Yoshizawa, *ACS Omega*, 2020, **5**, 26211–26219.

14 S. Ogata, M. Uranagase, Y. Takahashi and T. Kishi, *J. Phys. Chem. B*, 2021, **125**, 8989–8996.

15 S. Ogata and M. Uranagase, *J. Phys. Chem. B*, 2023, **127**, 2629–2638. Erratum: S. Ogata and M. Uranagase, *J. Phys. Chem. B*, 2023, **127**, 6833–6834.

16 M. Laurien, B. Demir, H. Büttemeyer, A. S. Herrmann, T. R. Walsh and L. C. Ciacchi, *Macromolecules*, 2018, **51**, 3983–3993.

17 T. Miura, M. Funada, Y. Shimoi and H. Morita, *J. Phys. Chem. B*, 2019, **123**, 1161–1170.

18 D. G. Luchinsky, H. Hafiychuk, V. Hafiychuk, K. Chaki, H. Nitta, T. Ozawa, K. R. Wheeler, T. J. Prater and P. V. E. McClintock, *J. Polym. Sci.*, 2020, **58**, 2051–2061.

19 S. Yang, Z. Cui and J. A. Qu, *J. Phys. Chem. B*, 2014, **118**, 1660–1669.

20 M. Solar, *Comput. Mater. Sci.*, 2021, **186**, 110048.

21 G. D. Davis, *Surf. Interface Anal.*, 1993, **20**, 368–372.

22 G. W. Critchlow and D. M. Brewis, *Int. J. Adhes. Adhes.*, 1996, **16**, 255–275.

23 J. D. Minfold, *Handbook of Aluminum Bonding Technology and Data*, Marcel Dekker Inc., New York, 1993.

24 E. W. Thrall and R. W. Shannon, *Adhesive Bonding of Aluminum Alloys*, Marcel Dekker Inc., New York, 1985.

25 R. Boyes, *Adhesive Bonding of Stainless Steel: Strength and Durability (Ph. D. thesis)*, Sheffield Hallam University, UK, 1998.

26 Y. Takahashi, S. Yamamoto, D. Katsuno and Y. Murata, *KOBELCO Technol. Rev.*, 2024, **41**, 70–78.

27 Y. Ota and T. Kojima, *KOBELCO Technol. Rev.*, 2017, **35**, 61–64.

28 Y. R. Shen, *Nature*, 1989, **337**, 519–525.

29 Y. R. Shen, *Fundamentals of Sum-Frequency Spectroscopy*, Cambridge University Press, Cambridge, UK, 2016.

30 S. Yamaguchi, T. Takayama, Y. Goto, T. Otosu and T. Yagasaki, *J. Phys. Chem. Lett.*, 2022, **13**, 9649–9653.

31 Y. Nojima, T. Shimoaka, T. Hasegawa and T. Ishibashi, *J. Phys. Chem. C*, 2023, **127**, 12349–12356.

32 T. Iwahashi, H. Kishida, W. Zhou, D. Kim and Y. Ouchi, *J. Phys. Chem. B*, 2024, **128**, 5018–5029.

33 E. Kinoshita, W. Sung, S. Nihonyanagi, H. Okuyama and T. Tahara, *J. Phys. Chem. Lett.*, 2025, **16**, 1088–1094.

34 T. Miyamae, H. Akiyama, M. Yoshida and N. Tamaoki, *Macromolecules*, 2007, **40**, 4601–4606.

35 Z. Chen, *Prog. Polym. Sci.*, 2010, **35**, 1376–1402.

36 Y. Fang, B. Li, J. Yu, J. Zhou, X. Xu, W. Shao and X. Lu, *Surf. Sci.*, 2013, **615**, 26–32.

37 C. Zhang, J. N. Myers and Z. Chen, *Langmuir*, 2014, **30**, 12541–12550.

38 T. Miyamae and Y. Taga, *J. Adhesion*, 2018, **94**, 1155–1167.

39 T. Sato, H. Akiyama, S. Horiuchi and T. Miyamae, *Surf. Sci.*, 2018, **677**, 93–98.

40 T. Sato, S. Ise, S. Horiuchi, H. Akiyama and T. Miyamae, *Int. J. Adhes. Adhes.*, 2019, **93**, 76–82.

41 K. Sensui, T. Tarui, T. Miyamae and C. Sato, *Chem. Commun.*, 2019, **55**, 14833–14836.

42 T. Lin, Y. Wu, E. Santos, X. Chen, D. Ahn, C. Mohler and Z. Chen, *Langmuir*, 2020, **36**, 15128–15140.

43 Y. Wu, T. Lin, E. Santos, D. Ahn, R. Marson, P. Sarker, X. Chen, F. Gubbels, N. Shephard, C. Mohler, T. Wei, T. Kuo and Z. Chen, *Soft Matter*, 2024, **20**, 4765–4775.

44 Y. Liu, Y. Shigemoto, T. Hanada, T. Miyamae, K. Kawasaki and S. Horiuchi, *ACS Appl. Mater. Interfaces*, 2021, **13**, 11497–11506.

45 F. M. Fowkes and M. A. Mostafa, *Ind. Eng. Chem. Prod. Res. Dev.*, 1978, **17**, 3–7.

46 A. Kurian, S. Prasad and A. Dhinojwala, *Langmuir*, 2010, **26**, 17804–17807.

47 S. Prasad, H. Zhu, A. Kurian, I. Badge and A. Dhinojwala, *Langmuir*, 2013, **29**, 15727–15731.

48 M. C. Wilson, S. Singla, A. J. Stefin, S. Kaur, J. V. Brown and A. Dhinojwala, *J. Phys. Chem. C*, 2019, **123**, 18495–18501.

49 S. Singla, M. C. Wilson and A. Dhinojwala, *Phys. Chem. Chem. Phys.*, 2019, **21**, 2513–2518.

50 R. S. Drago and B. B. Wayland, *J. Am. Chem. Soc.*, 1965, **87**, 3571–3576.

51 R. M. Badger and S. H. Bauer, *J. Chem. Phys.*, 1937, **5**, 839–851.

52 A. Franquet, H. Terryn and J. Vereecken, *Surf. Interface Anal.*, 2004, **36**, 681–684.

53 Nagase CemteX, Adhesive, https://group.nagase.com/nagasechemtex/e1/en/electric-structural-epoxy/adhesive-epoxy/, (accessed 2025-10-21).

54 S. Yamazaki, T. Aizawa and T. Miyamae, *ACS Omega*, 2025, **10**, 17468–17475.

55 T. Ohwaki, *R&D, Res. Dev.*, 2000, **50**, 70–73.

56 J. Quinton, L. Thomsen and P. Dastoor, *Surf. Interface Anal.*, 1997, **25**, 931–936.

57 D. G. Kurth and T. Bein, *Langmuir*, 1995, **11**, 3061–3067.

58 G. Pan and D. W. Schaefer, *Thin Solid Films*, 2006, **503**, 259–267.

59 S. Yamamoto, R. Kuwahara, A. Shundo and K. Tanaka, *ACS Appl. Polym. Mater.*, 2020, **2**, 1474–1481.

60 S. Yamamoto and K. Tanaka, *Soft Matter*, 2021, **17**, 1359–1367.

61 S. Yamamoto, R. Kuwahara and K. Tanaka, *ACS Appl. Polym. Mater.*, 2022, **4**, 6038–6046.

62 K. Harris, C. R. Wand, P. Visser and F. R. Siperstein, *RSC Appl. Interfaces*, 2024, **1**, 812–820.

63 J. M. Headrick, E. G. Diken, R. S. Walters, N. I. Hammer, R. A. Christie, J. Cui, E. M. Myshakin, M. A. Duncan, M. A. Johnson and K. D. Jordan, *Science*, 2005, **308**, 1765–1769. Erratum: J. M. Headrick, E. G. Diken, R. S. Walters, N. I. Hammer, R. A. Christie, J. Cui, E. M. Myshakin, M. A. Duncan, M. A. Johnson and K. D. Jordan, *Science*, 2005, **309**, 1326.

64 M. P. Allen and D. J. Tildesley, *Computer Simulation of Liquids*, Oxford University Press, 2nd edn, 2017, pp. 1–626.

65 H. Flyvbjerg and H. G. Petersen, *J. Chem. Phys.*, 1989, **91**, 461–466.

66 C. Turner, B. C. Donose, Kezia, G. Birkett and S. Pratt, *Water Res.*, 2020, **168**, 115135.